





Spin rectification effects in ferromagnetic metal microstrips induced by anisotropic magnetoresistance, planar Hall effect, and anomalous Hall effect

Kang He,¹ Jun Cheng ,¹ Man Yang,¹ Liang Sun,^{1,2} Wei Sun,³ Subhankar Bedanta ,⁴ Antonio Azevedo,⁵ Bingfeng Miao ,^{1,2,*} and Haifeng Ding ^{1,2}

¹*National Laboratory of Solid State Microstructures and Department of Physics, Nanjing University, Nanjing 210093, People's Republic of China*

²*Collaborative Innovation Center of Advanced Microstructures, Nanjing 210093, People's Republic of China*

³*BGRIMM Technology Group Co. LTD, Beijing 100160, People's Republic of China*

⁴*Laboratory for Nanomagnetism and Magnetic Materials (LNMM), School of Physical Sciences, National Institute of Science Education and Research (NISER), An OCC of Homi Bhabha National Institute (HBNI), Jatni-752050, India*

⁵*Departamento de Física, Universidade Federal de Pernambuco, Recife, Pernambuco 50670-901, Brazil*



(Received 7 July 2022; revised 22 August 2022; accepted 24 August 2022; published 8 September 2022)

Spin rectification effect (SRE) is an important electrical detection tool employed to probe magnetic dynamics and spin-orbit torques, and it is also closely related to spin pumping measurements. The SRE has multiple physical origins, and the entanglement among them makes it difficult to derive quantitative information. Herein, we present a systematic study of the SRE in $\text{Co}_{40}\text{Fe}_{40}\text{B}_{20}$ and Ni microstrips with out-of-plane-dominant microwave magnetic field excitation. The SREs from different physical mechanisms can be quantitatively decomposed via a symmetry consideration. The validity of the method is further supported by angular-dependent analyses. We observe both the anisotropic magnetoresistance induced SRE from the longitudinal induction current, and the planar Hall effect as well as the anomalous Hall effect induced SREs from the transverse induction current. Our work provides a comprehensive understanding of the SREs in ferromagnetic metal microstrips, and it is beneficial for quantitative analyses in microwave-related studies in spintronics.

DOI: [10.1103/PhysRevB.106.104407](https://doi.org/10.1103/PhysRevB.106.104407)

I. INTRODUCTION

A microwave magnetic field can drive the magnetization precession of a ferromagnet, which reaches its maximum amplitude at the ferromagnetic resonance (FMR) condition. In a ferromagnetic metal (FM), the precession of the magnetization induces a dynamic resistance change due to the anisotropic magnetoresistance (AMR), the planar Hall effect (PHE), and the anomalous Hall effect (AHE) since they are magnetization-orientation-dependent. In addition, the microwave also introduces induction currents in the FM. The coupling between the dynamic resistance and the dynamic induction current, which are of the same frequency, results in a dc rectified voltage, termed as the spin rectification effect (SRE) [1,2]. Due to its simple operation and high sensitivity, SRE measurement has become an important electrical technique to study the magnetic dynamics of FMs [3–6], spin waves [7–11] and domain walls [12,13], spin-orbit torques in magnetic bilayers [14–18], and magnetic tunnel junctions [19–23], and it can even be used to detect microwave magnetic fields [24,25]. The SRE typically contains both antisymmetric Lorentzian and symmetric Lorentzian components, and its symmetric Lorentzian component has the identical magnetic-field-dependence with the spin-to-charge conversion signals in the spin pumping measurements [26,27]. Distinguishing

the spin-to-charge conversion and SRE contributions is a challenging task, for which several methods have been developed [25–33].

Typically only the AMR induced SRE is considered in a microstrip (which is commonly used in the spin-orbit torque and the spin pumping measurements), as it is generally assumed that the dynamic induction current is confined along the strip only [14,17,25,27,28,31,33–37]. On the other hand, the PHE and AHE induced SREs were less frequently addressed [2,38–42]. As will be given in detail below, the distribution of the induction current may bring in SREs from different physical origins. Under certain circumstances, the PHE and AHE induced SREs can have similar or even larger amplitudes than that of the AMR induced SRE. For instance, we have recently reported the PHE induced SRE in Permalloy (Py) microstrip with comparable magnitude to the widely studied AMR induced SRE [43]. Therefore, a more comprehensive understanding of the mechanisms of SREs in FMs is highly desired.

In this work, we perform a systematic study of the SREs in single-layer Ni and $\text{Co}_{40}\text{Fe}_{40}\text{B}_{20}$ (CoFeB) microstrips, including the SREs with AMR, PHE, and AHE origins. We focus on the geometry where the sample is placed in the gap between a signal line and one of the ground lines of a coplanar waveguide (CPW) [Fig. 1(a)], in which the out-of-plane microwave magnetic field h_z is dominant [44]. Since its first usage in spin pumping measurement [25], this geometry has become one of the most widely used configurations [2,45].

*Corresponding author: bfmiao@nju.edu.cn

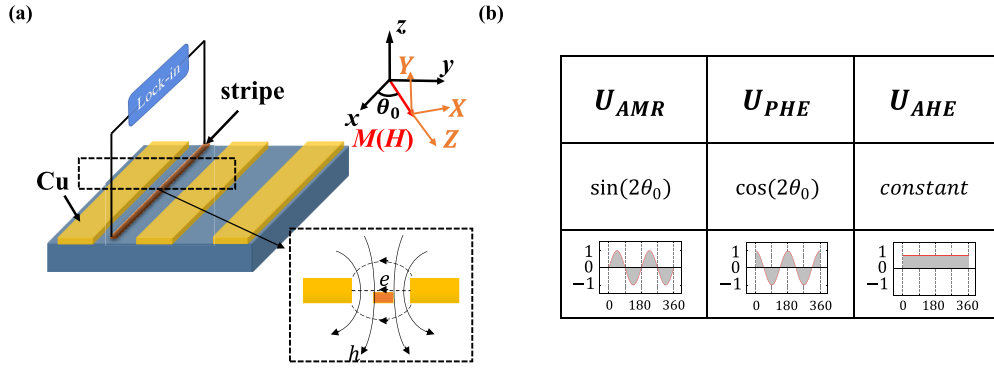


FIG. 1. (a) Schematic of the measurement geometry with a $2 \text{ mm} \times 40 \mu\text{m}$ ferromagnetic metal microstrip placed in the gap between the signal line and one of the ground lines of a CPW. θ_0 defines the angle between the static magnetic field H and the long axis of the strip. Inset: the schematic of the cross-section view of the microwave electromagnetic field distribution in the gap. (b) In-plane magnetic field angular dependences and the corresponding sketches of SREs due to AMR, PHE, and AHE in this measurement configuration.

Ni and CoFeB are FMs commonly used in spintronic studies with very different relative weights in AMR and AHE [33,46]. We develop a method to quantitatively decompose the AMR, PHE, and AHE induced SREs based on a simple symmetry operation. The validity of the method is further supported by the angular-dependent measurements. We find that the SREs from different origins are comparable with each other for the Ni microstrip, while the AHE induced SRE is an order of magnitude larger than those induced by the AMR and the PHE in CoFeB. Quantitative agreements are also established between the experiments and the theoretical model. Our findings demonstrate that not only the AMR induced SRE but also the PHE and AHE induced SREs need to be considered. As the SREs from different origins are sensitive to the magnetization components along different directions, a full understanding of SREs in FMs benefits both studies of magnetic dynamics and spin current detections with the spin pumping technique. For instance, a vectorial investigation of the spin dynamics may be enabled via the component resolved SRE measurements.

II. GENERAL DESCRIPTIONS OF DIFFERENT SREs IN FM MICROSTRIPS

Under microwave excitation with an angular frequency of ω , the rf dynamic magnetic field ($\mathbf{h}e^{i\omega t}$) exerts a field torque on the magnetization of the FM and drives it to precess around its equilibrium direction. This results in a dynamic magnetization $\mathbf{m} = \hat{\chi}\mathbf{h}$, where $\hat{\chi}$ is the Polder tensor [2,47]. When \mathbf{h} is along the z -direction and the in-plane dc external magnetic field H is at an angle θ_0 with respect to the long axis of the strip [Fig. 1(a)], we have [2,47]

$$m_z(t) = 0, \quad (1)$$

$$m_x(t) = \chi_0[A(H) - iS(H)]ih_z e^{i\omega t}, \quad (2)$$

$$m_y(t) = \chi_0[A(H) - iS(H)](\gamma H_0/\omega)h_z e^{i\omega t}. \quad (3)$$

Here, \vec{X} , \vec{Y} , and \vec{Z} are the moving coordinates, with \vec{Z} along the equilibrium direction of the magnetization \vec{M} , and $\vec{X} = \vec{z} \times \vec{Z}$, $\vec{Y} = \vec{Z} \times \vec{X}$, with the xyz coordinate fixed with respect to the sample, as shown in Fig. 1(a). $m_i(t)$ is the

component of the dynamic magnetization in the moving coordinate axis (i could be X , Y , or Z), γ is the gyromagnetic ratio, $\chi_0 = \frac{M_0}{\alpha(M_{\text{eff}} + 2H_0)}$, with M_0 being the amplitude of the magnetization, H_0 is the resonance field, and α is the damping factor, respectively. In addition, $M_{\text{eff}} = M_0 + \frac{2K_S}{\mu_0 M_0}$ is the effective magnetization, K_S is the surface anisotropy energy density, and μ_0 is the vacuum permeability, respectively. M_{eff} can be obtained from the frequency-dependent resonance field via the fitting with the Kittel formula $\omega = \gamma\sqrt{H_0(H_0 + M_{\text{eff}})}$. Since $\frac{2K_S}{\mu_0 M_0}$ is relatively small as compared to M_0 , the value of M_0 is usually taken as the value of M_{eff} in the calculation. $S(H) = \frac{(\Delta H)^2}{(H - H_0)^2 + (\Delta H)^2}$ and $A(H) = \frac{\Delta H(H - H_0)}{(H - H_0)^2 + (\Delta H)^2}$ define the symmetric and antisymmetric Lorentzian components, respectively. The relative phase Θ between \mathbf{h} and \mathbf{m} can thus be described by $\Theta = \arctan[S(H)/A(H)] = \arctan[\Delta H/(H - H_0)]$ [48].

In the gap between the signal line and one of the ground lines of a CPW [Fig. 1(a)], in addition to the out-of-plane microwave magnetic field h_z , there is also a microwave electric field perpendicular to the strip and along the y -direction. Therefore, two kinds of dynamic induction currents coexist in the sample: one is the typically considered dynamic current with density j_x along the strip due to the Faraday induction, another is the dynamic current with density j_y transverse to the strip due to Ohm's law from the microwave electric field. Thus, the possible SREs in this measurement configuration include the AMR induced SRE from j_x , and the PHE and the AHE induced SREs from j_y . The AMR of a polycrystalline FM can be expressed in the form of $\rho_{\text{AMR}}(\theta_0) = \rho(0) - \Delta\rho \sin^2\theta_0$, where θ_0 is the angle between the current and the magnetization direction, and $\Delta\rho = \rho_{\parallel} - \rho_{\perp}$ is the difference in the resistivity when the current and the magnetization are aligned (ρ_{\parallel}) and orthogonal (ρ_{\perp}) to each other. Meanwhile, the in-plane magnetization orientation dependent resistivity measured transverse to the current direction also results in the PHE in the form of $\rho_{\text{PHE}}(\theta_0) = \frac{\Delta\rho}{2} \sin(2\theta_0)$. The coupling between the PHE and j_y results in a rectified voltage along the strip [2,38]. Furthermore, the precession of the magnetization also causes a nonzero component of the magnetization perpendicular to the plane. This generates an anomalous Hall effect (AHE), which is proportional to the anomalous Hall resistivity ρ_{AHE} . When it is coupled with j_y , it also contributes

a rectified voltage along the strip [2,38]. Therefore, the rectified voltages along the strip can be expressed by the following equations:

$$U_{\text{AMR}} = \langle j_x(t) \Delta \rho [m_x(t)]^2 L \rangle \\ = U_{\text{AMR}}^0 \sin(2\theta_0) [-A(H) \sin \psi_x - S(H) \cos \psi_x], \quad (4)$$

$$U_{\text{PHE}} = \langle j_y(t) \Delta \rho m_x(t) m_y(t) L \rangle \\ = U_{\text{PHE}}^0 \cos(2\theta_0) [A(H) \sin \psi_y + S(H) \cos \psi_y], \quad (5)$$

$$U_{\text{AHE}} = \langle -j_y(t) \rho_{\text{AHE}} m_z(t) L \rangle \\ = U_{\text{AHE}}^0 [-A(H) \cos \psi_y + S(H) \sin \psi_y]. \quad (6)$$

Here, $j_x(t) = j_x e^{i(\omega t + \psi_x)}$, $j_y(t) = j_y e^{i(\omega t + \psi_y)}$ are the current densities of the induction currents along the x - and y -directions, respectively, L is the length of the strip along the measurement leads, and ψ_x (ψ_y) is the relative phase between j_x (j_y) and h_z , which is determined by the frequency-dependent microwave impedance of the circuits [48]. When only h_z is considered, it can be easily derived that [2,38,47]

$$U_{\text{AMR}}^0 = \frac{j_x \Delta \rho L}{2M_0} \chi_0 h_z, \quad U_{\text{PHE}}^0 = \frac{j_y \Delta \rho L}{2M_0} \chi_0 h_z, \\ U_{\text{AHE}}^0 = \frac{j_y \rho_{\text{AHE}} L}{2M_0} \frac{\gamma H_0}{\omega} \chi_0 h_z. \quad (7)$$

From Eqs. (4)–(7), it can be concluded that U_{AMR} , U_{PHE} , and U_{AHE} are all symmetric with the static in-plane magnetic field, i.e., $U(\theta_0^{+H}) = U(\theta_0^{-H})$ in the configuration shown in Fig. 1(a).

Figure 1(b) summarizes the angular dependences of different rectified voltages. Among them, U_{AHE} is independent of the direction of the in-plane external static field. At $\theta_0 = 0^\circ$ and 90° , U_{AMR} disappears while U_{PHE} reaches its maximum with the same magnitude but the opposite sign. Similarly, at $\theta_0 = 45^\circ$ and 135° , U_{PHE} vanishes and U_{AMR} reaches its maximum with the same magnitude but the opposite sign. These features provide an easy approach to decompose different components of SRE through the basic symmetry operation, namely

$$U_{\text{PHE}} = \frac{U(0^\circ) - U(90^\circ)}{2}, \quad U_{\text{AHE}} = \frac{U(0^\circ) + U(90^\circ)}{2}, \quad (8)$$

and

$$U_{\text{AMR}} = \frac{U(45^\circ) - U(135^\circ)}{2}, \quad U_{\text{AHE}} = \frac{U(45^\circ) + U(135^\circ)}{2}. \quad (9)$$

Thus, through the measurements at four specific angles of $\theta_0 = 0^\circ$, 45° , 90° , and 135° , we can readily separate the SRE components with different physical origins, and U_{AHE} obtained with two independent approaches can serve as a consistent check of the proposed method. We note that the resonance field is slightly different at different θ_0 due to the shape anisotropy. At a frequency of several GHz, this difference is about 1–2 % for Ni and CoFeB. To accommodate the potential

influence, one can first fit the field-dependent data with the Lorentzian functions at different θ_0 and use the fitted results to perform the symmetry operation as mentioned above.

III. EXPERIMENTAL RESULTS AND DISCUSSIONS

10-nm-thick Ni and CoFeB single layers are deposited on thermally oxidized Si substrates with dc magnetron sputtering. The films are subsequently covered with 15-nm SiN as the protecting layer by the rf magnetron sputtering *in situ*. The samples are further patterned into strips with lateral dimensions of $2 \text{ mm} \times 40 \mu\text{m}$ using the photolithography and lift-off techniques. Ni and CoFeB microstrips are placed in the center of the gap between the signal line and one of the ground lines of a CPW. The microwave with a fixed power of $\sim 320 \text{ mW}$ and variable frequency is fed into the CPW to excite the precession of the sample magnetization with h_z . To improve the signal-to-noise ratio, the microwave is modulated by a 13.37-kHz transistor-transistor logic (TTL) signal, and the voltages along the strips are detected with a lock-in amplifier. The modulation also minimizes the parasite signals caused by the thermal effect [49]. A rotatable static field H is applied within the sample plane, and all measurements are performed at room temperature.

Figures 2(a) and 2(b) present the static magnetic-field-dependent dc signals of Ni at three representative frequencies for $\theta_0 = 0^\circ$ and 90° , respectively. As discussed above, when the external field is applied along these two directions, U_{AMR} disappears and only U_{PHE} and U_{AHE} remain [Eqs. (4)–(6)]. It is interesting to note that U_{PHE} is in its maximum with equal amplitude but opposite sign, and U_{AHE} is the same at $\theta_0 = 0^\circ$ and 90° . The obtained signal can be decomposed into symmetric Lorentzian component U_S and antisymmetric Lorentzian component U_A with fitting $U = U_S S(H) + U_A A(H)$. The symmetric Lorentzian component is symmetric about the resonance field, and its sign is determined by the peak or dip value at the resonance field; the antisymmetric Lorentzian component is antisymmetric about the resonance field, and its sign “+” or “–” is determined by the evolution from “peak-to-dip” or “dip-to-peak,” respectively. Overall, we find that the symmetric Lorentzian components of the measured signals for $\theta_0 = 0^\circ$ have opposite signs to the signals for $\theta_0 = 90^\circ$ at 8 and 10 GHz, while they have the same sign at 13 GHz. In addition, the antisymmetric Lorentzian components have the opposite behavior. As will be discussed in the following, the sign evolution is mainly due to the evolution of the relative phase (ψ_y) between the transverse induction current (j_y) and the rf microwave magnetic field h_z . The slight asymmetry of the voltage signals between the positive and the negative magnetic fields may originate from the self-pumping induced inverse spin Hall effect in Ni itself [50,51] or the SRE induced by the rf magnetic field within the sample plane [43]. In this work, we mainly focus on the h_z excited SREs (symmetric with H). We thus use $U_{\text{SR}}(\theta_0) = \frac{U(\theta_0^{+H}) + U(\theta_0^{-H})}{2}$ to extract the SRE signals from h_z only [Figs. 2(c) and 2(d)]. Hereafter, all discussions are focused on the spin rectification contributions from h_z only.

We follow Eq. (8) to obtain U_{PHE} and U_{AHE} , respectively. The ratio between $\Delta \rho$ and ρ_{AHE} can then be calculated with

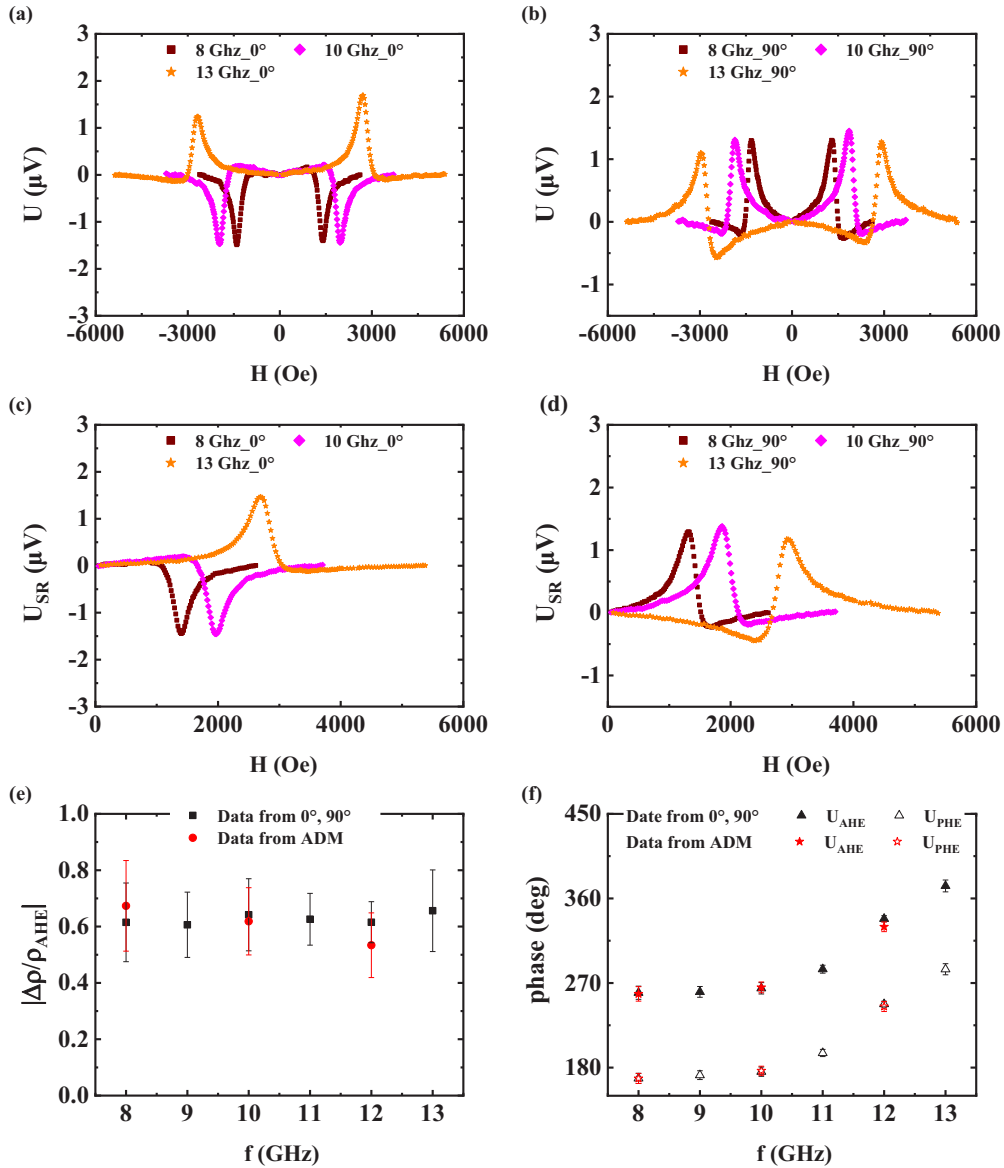


FIG. 2. (a), (b) H -dependent microwave excited voltages of Ni at three representative frequencies with H along $\theta_0 = 0^\circ$ and 90° , respectively. (c), (d) H -dependent spin rectification contributions from h_z extracted from data in (a) and (b). (e) The amplitudes of $\Delta\rho/\rho_{\text{AHE}}$ at different frequencies obtained from 0° and 90° data (black squares) and from the angular-dependent measurements (ADM, red circles). (f) The phases of U_{PHE} and U_{AHE} at different frequencies obtained from 0° and 90° data (black triangles) and from ADM (red pentagrams).

$|\frac{\Delta\rho}{\rho_{\text{AHE}}}| = |\frac{U_{\text{PHE}}^0}{U_{\text{PHE}}^S}| \sqrt{1 + \frac{M_{\text{eff}}}{H_0}}$, which should be an intrinsic parameter of the Ni film and irrespective of the microwave frequency. Figure 2(e) presents the calculated $|\frac{\Delta\rho}{\rho_{\text{AHE}}}|$ at different frequencies (black squares) from the SREs obtained with $\theta_0 = 0^\circ$ and 90° , respectively. It shows roughly a constant ($\sim 0.63 \pm 0.16$). This value is also consistent with that obtained with the dc measurement (see Appendix A).

The symmetric and antisymmetric Lorentzian components of U_{PHE} and U_{AHE} can be expressed as $(\frac{U_{\text{PHE}}^S}{U_{\text{PHE}}^A}) = U_{\text{PHE}}^0 \cos(2\theta_0) \begin{pmatrix} \cos\psi_y \\ \sin\psi_y \end{pmatrix}$ and $(\frac{U_{\text{AHE}}^S}{U_{\text{AHE}}^A}) = U_{\text{AHE}}^0 \begin{pmatrix} \sin\psi_y \\ -\cos\psi_y \end{pmatrix}$, respectively. Typically, the PHE (AMR) of polycrystalline ferromagnetic metal is positive. Thus, ψ_y can be obtained from the phase of PHE induced SRE with $\arctan(U_{\text{PHE}}^A/U_{\text{PHE}}^S) = \psi_y$. Depending on the sign of AHE, the phase of AHE induced

SRE can be $\arctan(U_{\text{AHE}}^A/U_{\text{AHE}}^S) = \psi_y \pm \frac{\pi}{2}$. Since Ni has negative AHE (see Appendix A), we have $\arctan(U_{\text{AHE}}^A/U_{\text{AHE}}^S) = \psi_y + \frac{\pi}{2}$ for Ni. The experimentally obtained phases of U_{PHE} and U_{AHE} at different frequencies obtained from 0° and 90° data are plotted in Fig. 2(f), respectively. We find that although the phases in U_{PHE} and U_{AHE} change with frequency dramatically, their differences are indeed roughly fixed at 90° . The 90° phase shift is consistent with the scenario of the PHE and the AHE, as they originate from the in-plane and out-of-plane dynamic magnetization of FM, respectively [Eqs. (5) and (6)]. For Ni, U_{PHE}^0 is comparable to U_{AHE}^0 with $|\frac{\Delta\rho}{\rho_{\text{AHE}}}| \sim 0.63$. As the phase ψ_y increases roughly from 180° to 270° with increasing frequency [Fig. 2(f)], $(\frac{U_{\text{PHE}}^S}{U_{\text{PHE}}^A})$ dominates in the total signal at low frequency, and $(\frac{U_{\text{AHE}}^S}{U_{\text{PHE}}^A})$ dominates in the total

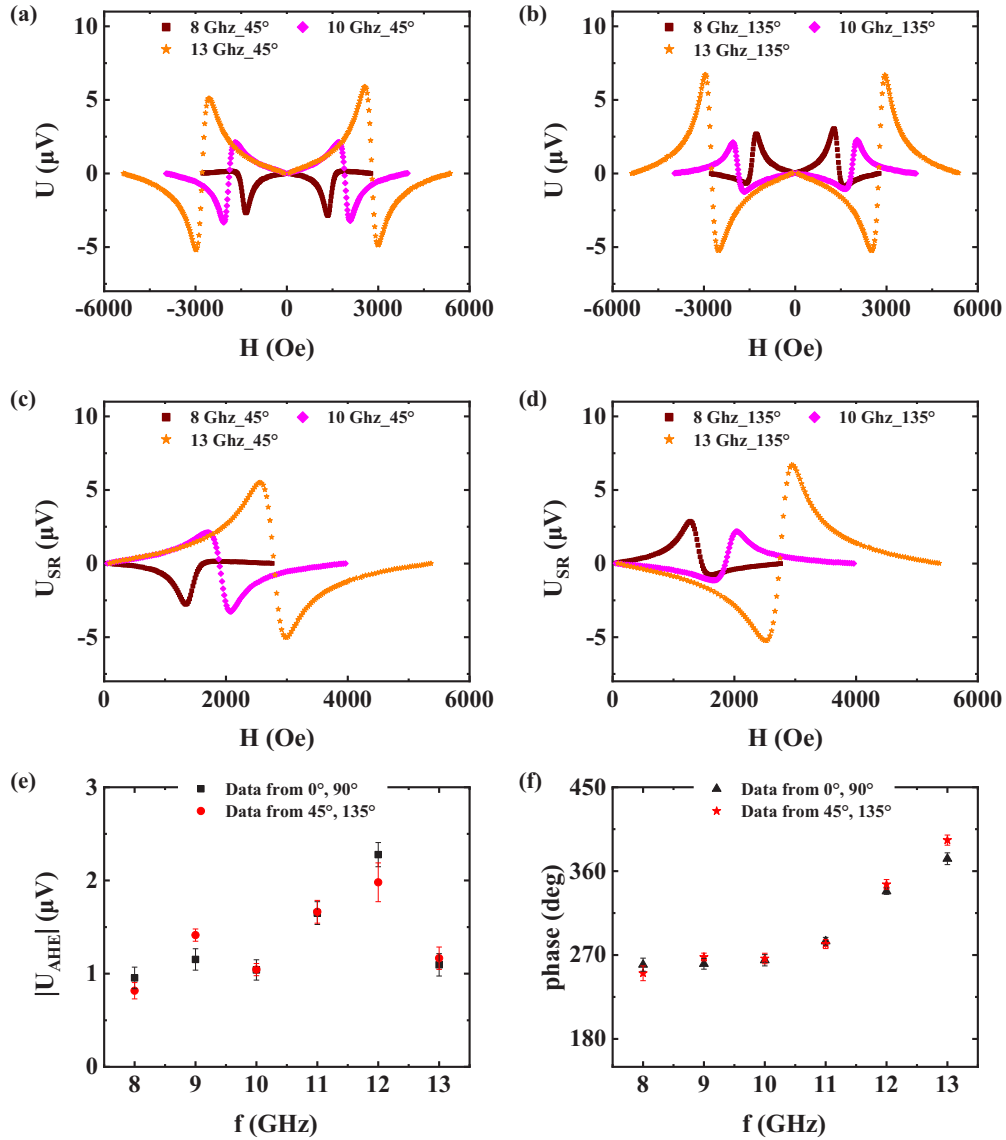


FIG. 3. (a), (b) H -dependent microwave excited voltages of Ni at three representative frequencies with H along $\theta_0 = 45^\circ$ and 135° , respectively. (c), (d) H -dependent spin rectification contributions from h_z extracted from data in (a) and (b). (e) Amplitudes of the AHE induced SRE contributions, and (f) phases of U_{AHE} at different frequencies obtained from $\theta_0 = 0^\circ$ and 90° data [black squares in (e) and black triangles in (f)] and from $\theta_0 = 45^\circ$ and 135° data [red circles in (e) and red pentagrams in (f)].

signal at high frequency. This argument explains qualitatively the evolution of the sign change in Figs. 2(a)–2(d) at different frequencies.

Figures 3(a) and 3(b) present the static magnetic-field-dependent dc signals of Ni at three representative frequencies for $\theta_0 = 45^\circ$ and 135° . And Figs. 3(c) and 3(d) are the h_z excited spin rectification contributions extracted from data in (a) and (b) by the same operation as in Fig. 2. Because the PHE induced SRE disappears for $\theta_0 = 45^\circ$ and 135° , one can use Eq. (9) to obtain the AHE induced SRE as well as the AMR induced SRE. Similarly, because the AMR induced SRE disappears for $\theta_0 = 0^\circ$ and 90° (Fig. 2), one can use Eq. (8) to obtain the AHE induced SRE as well as the PHE induced SRE. The decomposed amplitudes and phases of U_{AHE} obtained from $\theta_0 = 45^\circ$ and 135° (red data points) at

different frequencies are plotted in Figs. 3(e) and 3(f). They are almost the same as those obtained with $\theta_0 = 0^\circ$ and 90° (black data points). This consistency evidences the validity of the proposed method for decomposing the SREs from different physical origins.

To further depict the features of different SREs, we perform the full in-plane angular-dependent SRE measurements at two representative frequencies. The raw data for the H -dependent microwave excited voltages of Ni at different field directions for 10 GHz are presented in Appendix B. The angular-dependent symmetric Lorentzian component U_S and the antisymmetric Lorentzian component U_A of a 10-nm Ni strip at a frequency of 10 GHz are presented as the black symbols in Figs. 4(a) and 4(b), respectively. The experimental data can be well fitted by considering the SRE contributions

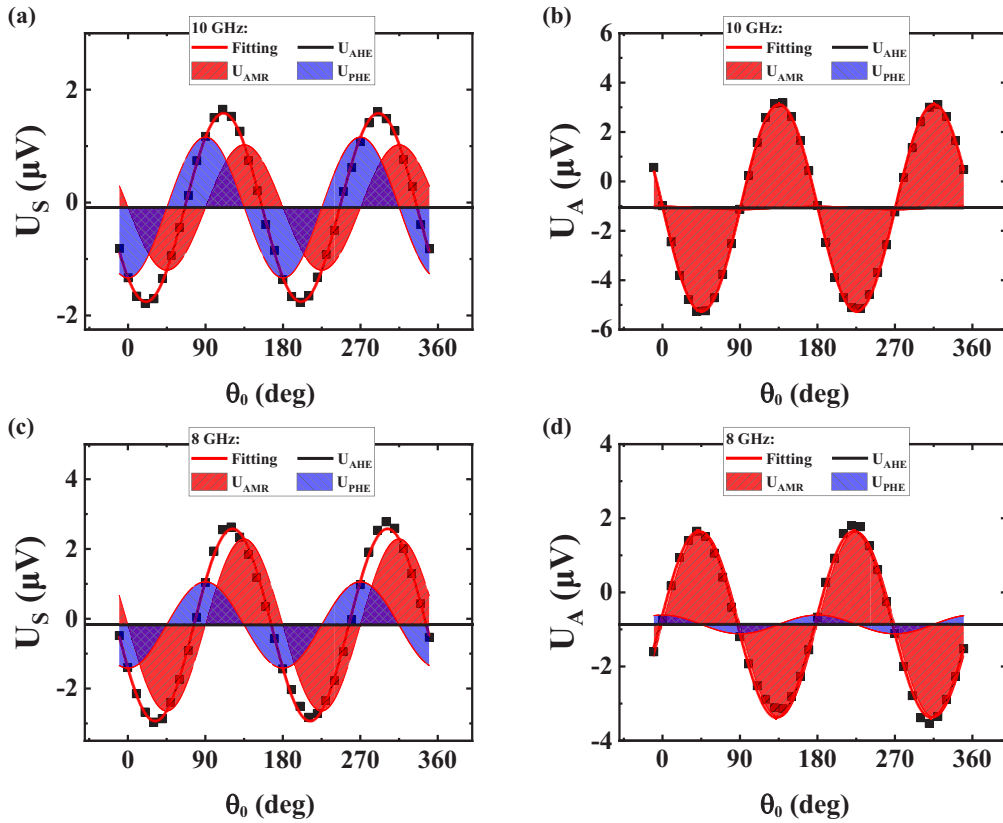


FIG. 4. The angular-dependent symmetric Lorentzian component U_S (a), (c) and antisymmetric Lorentzian component U_A (b), (d) for Ni at two representative frequencies of 10 and 8 GHz, respectively. The black symbols are the experimental data, and the red curves are the fittings. The red and blue shadowed areas and the black horizontal line denote the components of AMR, PHE, and AHE induced SREs, respectively.

from AMR, PHE, and AHE:

$$U_{S(A)} = U_{\text{AMR}}^{S(A)} \sin(2\theta_0) + U_{\text{PHE}}^{S(A)} \cos(2\theta_0) + U_{\text{AHE}}^{S(A)}, \quad (10)$$

where the red (blue) shadowed areas and the black horizontal line represent the components of the AMR (PHE) and AHE induced rectification signals, respectively. The vanishing antisymmetric Lorentzian component U_{PHE}^A indicates the phase between the microwave magnetic field h_z and the transverse induction current density j_y , $\psi_y = 180^\circ$ [Fig. 4(b) blue shadow]. Due to the 90° phase shift between U_{PHE} and U_{AHE} , we find that the AHE induced SRE is dominated by the antisymmetric Lorentzian component [Figs. 4(a) and 4(b) black horizontal lines]. Changing the frequency to 8 GHz, U_{PHE}^A emerges albeit with a relatively small amplitude [Fig. 4(d)]. Equally important, the experimental data at 8 GHz can also be well fitted with Eq. (10) [Figs. 4(c) and 4(d)], validating our analysis method. We can further use the fitted symmetric Lorentzian components and antisymmetric Lorentzian components of PHE and AHE induced SREs to calculate the $|\frac{\Delta\rho}{\rho_{\text{AHE}}}|$ as well as the phases of U_{AHE} and U_{PHE} . The results are plotted in Fig. 2(e) (red circles) and Fig. 2(f) (red pentagrams), and they are all in good agreement with the values obtained from the symmetry analysis based on the signals obtained at the four specific angles mentioned above [Figs. 2(e) and 2(f)].

In the Ni microstrip, we do observe three different SREs, and the experimental results are in good agreement with the theory. The rectified voltage due to the AHE, however, is

relatively small as compared to those originating from the AMR and PHE. We next perform similar studies on CoFeB, in which the AHE coefficient is significantly larger than the PHE coefficient [33] (also see Appendix A). Figures 5(a) and 5(b) present the static magnetic-field-dependent dc signals of CoFeB at three representative frequencies for $\theta_0 = 0^\circ$ and 90° , and Figs. 5(c) and 5(d) are the h_z excited spin rectification contributions extracted from data in (a) and (b). At first glance, we find that both the magnitude and the line shape of the voltage curves for $\theta_0 = 0^\circ$ and 90° are similar for all frequencies. Such similarity indicates that the rectified voltage contribution of AHE is dominant over that of PHE, as the latter changes sign between $\theta_0 = 0^\circ$ and 90° (AMR induced SRE is vanishing at these two specific directions). We also performed the in-plane angular-dependent measurement for the CoFeB at 10 GHz (see Appendix B for the raw data at different field directions), with the symmetric Lorentzian component U_S presented in Fig. 5(e) and the antisymmetric Lorentzian component U_A presented in Fig. 5(f). Again, the data can be well fitted by Eq. (10), with a distinct offset of the voltage U_A coming from the AHE induced SRE [Fig. 5(f)]. And as the AHE of CoFeB is overwhelmingly large (Appendix A), the spin rectification contribution from AHE dominates over the spin rectification contributions from AMR and PHE in CoFeB. We thus unambiguously demonstrated the PHE and AHE induced SREs due to the transverse induction current in both Ni and CoFeB microstrips, with quantitative agreement between the experiments and the theory.

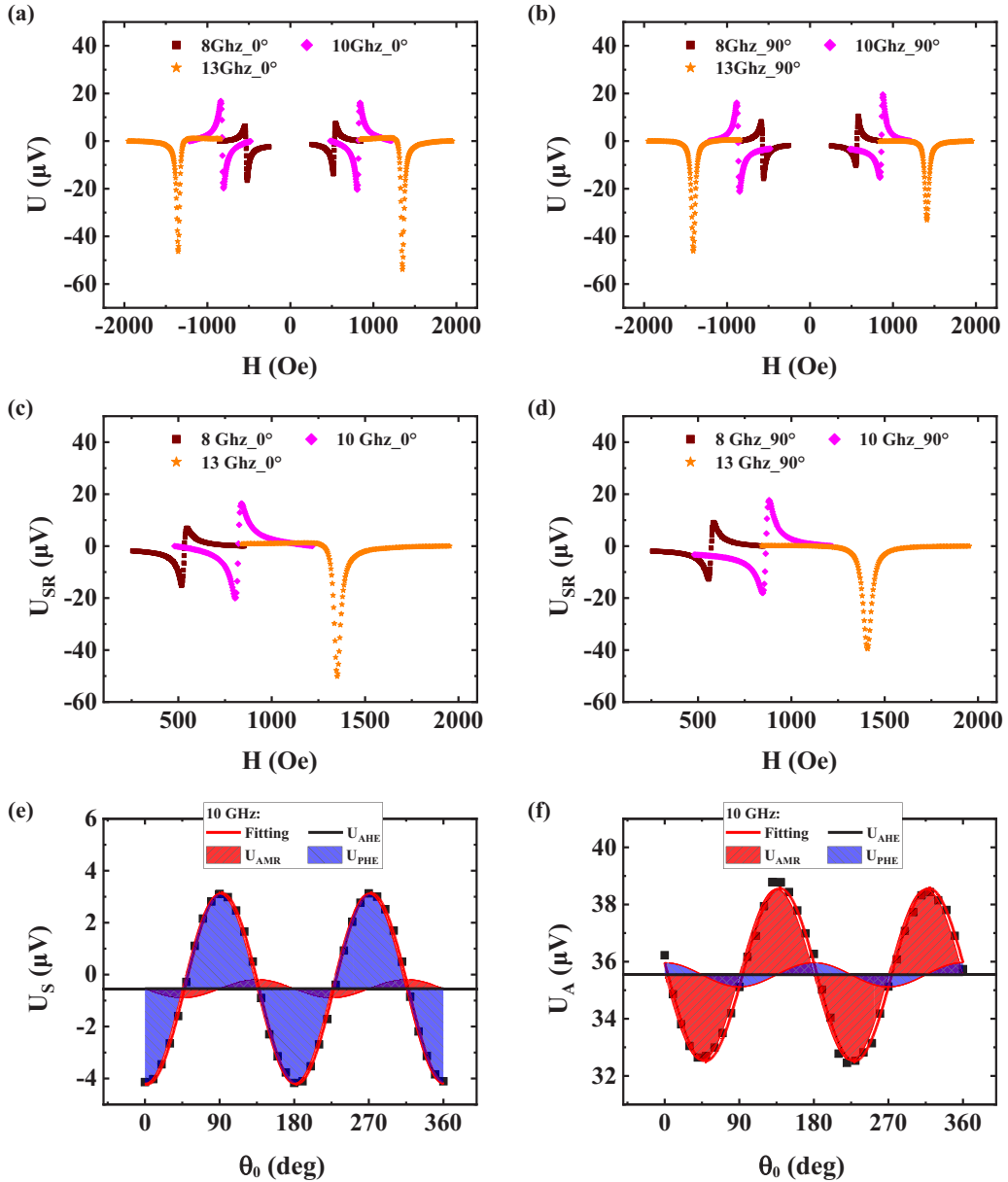


FIG. 5. (a), (b) H -dependent microwave excited voltages of CoFeB at three representative frequencies with H along $\theta_0 = 0^\circ$ and 90° , respectively. (c), (d) H -dependent spin rectification contributions from h_z extracted from data in (a) and (b). (e), (f) The angular-dependent symmetric Lorentzian component U_S and the antisymmetric Lorentzian component U_A for CoFeB at 10 GHz, respectively.

IV. SUMMARY

In this work, we performed a systematic study on the spin rectifications of ferromagnetic metallic microstrips with dominant perpendicular rf magnetic field microwave excitation. In addition to the SRE due to the AMR through the generally recognized longitudinal induction current along the strip, we explicitly observed the SREs from PHE and AHE from the transverse induction current. We find that SREs due to the transverse induction current may have dominant contributions in the measured SRE signals, even when the aspect ratio of length/width is large (50 in this study). Based on symmetry analysis, we developed a simple but consistent method to quantitatively separate the AMR, PHE, and AHE induced contributions in the measured SRE signals. And the validity of the

method is further supported by the angular-dependent studies. Moreover, since the AMR, PHE, and AHE induced SREs are sensitive to the magnetization along different directions, the separation of different contributions may enable an effective tool to investigate the spin dynamics in a vectorial manner.

ACKNOWLEDGMENTS

This work was supported by the National Key R&D Program of China (Grants No. 2021YFB3502400 and No. 2018YFA0306004), the National Natural Science Foundation of China (Grants No. 51971110, No. 11974165, No. 11734006, and No. 92165103), and the Natural Science Foundation of Jiangsu Province (Grant No. BK20190057).

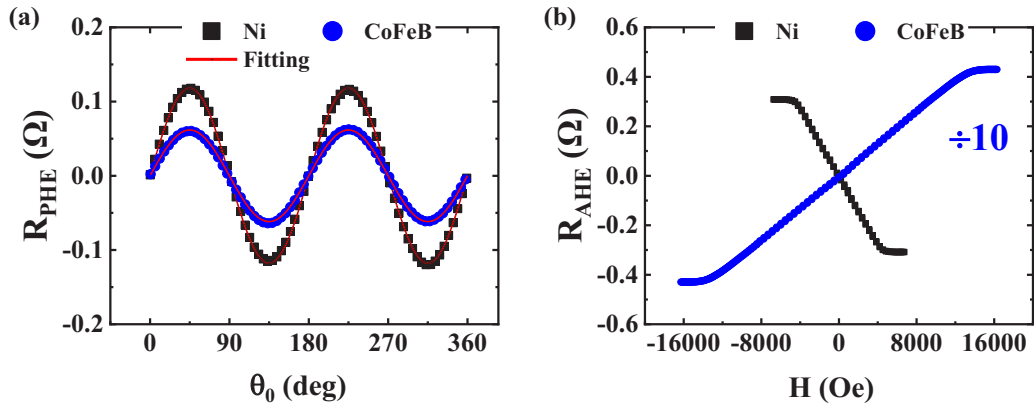


FIG. 6. (a) Angular dependent PHE of 10-nm Ni (black) and 10-nm CoFeB (blue), where the red lines are fitting with $\sin \theta \cos \theta$. (b) AHE of Ni (black) and CoFeB (blue), where the linear backgrounds from the ordinary Hall effect have been subtracted. Note: the AHE of CoFeB has been divided by 10.

APPENDIX A: PHE AND AHE OF Ni AND CoFeB

Figure 6 presents the PHE and AHE of 10-nm Ni and CoFeB. Indeed, we find that PHE and AHE are comparable for Ni, and AHE is dominant for CoFeB. For Ni, $|\frac{\Delta\rho}{\rho_{\text{AHE}}}|$ is 0.77 from the dc measurements, and this value is consistent with our estimation from SRE within the error bar. For CoFeB, $|\frac{\Delta\rho}{\rho_{\text{AHE}}}|$ is 0.029 from the dc measurements, and the PHE is nearly two orders of magnitude smaller than its AHE.

APPENDIX B: RAW DATA OF H -DEPENDENT MICROWAVE EXCITED VOLTAGES OF Ni AND CoFeB AT DIFFERENT FIELD DIRECTIONS FOR 10 GHz

Figure 7 presents the raw data for the H -dependent microwave excited voltages of 10-nm Ni [Fig. 7(a)] and 10-nm

CoFeB [Fig. 7(b)] at different field directions for 10 GHz. One can notice that the SRE in Ni shows an apparent angular dependence, suggesting the considerable contributions from the AMR and PHE induced mechanisms. On the other hand, the SRE in CoFeB shows almost no angular dependence, evidencing that the AHE induced SRE is overwhelmingly dominant. For each direction, similar to what we did in Figs. 2 and 3, we first perform $U_{\text{SR}}(\theta_0) = \frac{U(\theta_0^{+H}) + U(\theta_0^{-H})}{2}$ to obtain the SRE due to h_z . Then, the symmetric and antisymmetric components can be obtained via fitting with the equation $U = U_S \frac{(\Delta H)^2}{(H-H_0)^2 + (\Delta H)^2} + U_A \frac{\Delta H(H-H_0)}{(H-H_0)^2 + (\Delta H)^2}$. The obtained U_S and U_A can be perfectly fitted by Eq. (10), as presented in Figs. 4, 5(e), and 5(f).

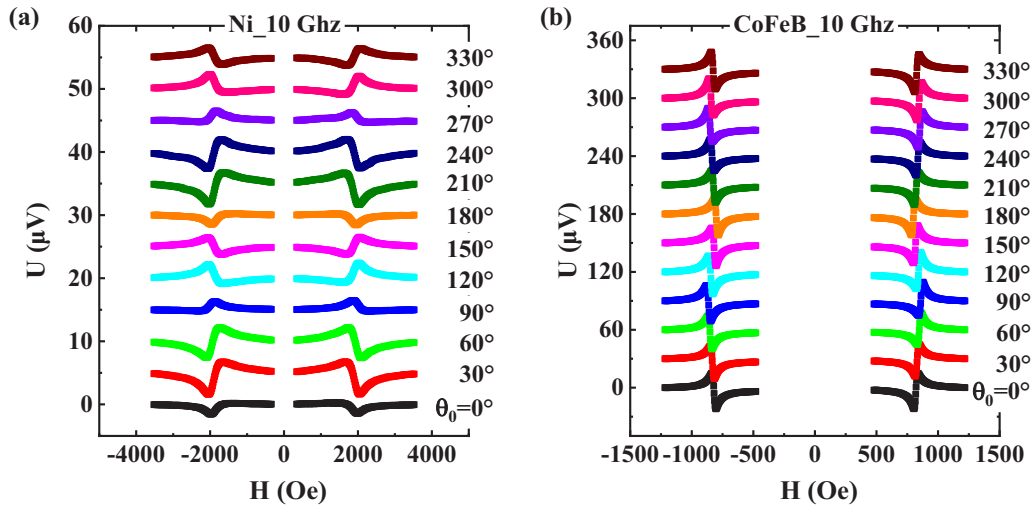


FIG. 7. H -dependent microwave excited voltages of (a) 10-nm Ni and (b) 10-nm CoFeB at different field directions for 10 GHz. The curves have been shifted vertically for clarity.

- [1] Y. S. Gui, N. Mecking, X. Zhou, G. Williams, and C. M. Hu, *Phys. Rev. Lett.* **98**, 107602 (2007).
- [2] M. Harder, Y. Gui, and C.-M. Hu, *Phys. Rep.* **661**, 1 (2016).
- [3] Y. S. Gui, S. Holland, N. Mecking, and C. M. Hu, *Phys. Rev. Lett.* **95**, 056807 (2005).
- [4] M. V. Costache, S. M. Watts, M. Sladkov, C. H. van der Wal, and B. J. van Wees, *Appl. Phys. Lett.* **89**, 232115 (2006).
- [5] D. Choe, M.-J. Jin, S.-I. Kim, H.-J. Choi, J. Jo, I. Oh, J. Park, H. Jin, H. C. Koo, B.-C. Min, S. Hong, H.-W. Lee, S.-H. Baek, and J.-W. Yoo, *Nat. Commun.* **10**, 4510 (2019).
- [6] H. F. Legg, M. Rößler, F. Münnig, D. Fan, O. Breunig, A. Bliessener, G. Lippertz, A. Uday, A. A. Taskin, D. Loss, J. Klinovaja, and Y. Ando, *Nat. Nanotechnol.* **17**, 696 (2022).
- [7] M. Tsoi, A. G. M. Jansen, J. Bass, W. C. Chiang, V. Tsoi, and P. Wyder, *Nature (London)* **406**, 46 (2000).
- [8] S. I. Kiselev, J. C. Sankey, I. N. Krivorotov, N. C. Emley, R. J. Schoelkopf, R. A. Buhrman, and D. C. Ralph, *Nature (London)* **425**, 380 (2003).
- [9] Y. S. Gui, N. Mecking, and C. M. Hu, *Phys. Rev. Lett.* **98**, 217603 (2007).
- [10] Y. Li, W. Cao, V. P. Amin, Z. Zhang, J. Gibbons, J. Sklenar, J. Pearson, P. M. Haney, M. D. Stiles, W. E. Bailey, V. Novosad, A. Hoffmann, and W. Zhang, *Phys. Rev. Lett.* **124**, 117202 (2020).
- [11] Y. Li, C. Zhao, V. P. Amin, Z. Zhang, M. Vogel, Y. Xiong, J. Sklenar, R. Divan, J. Pearson, M. D. Stiles, W. Zhang, A. Hoffmann, and V. Novosad, *Appl. Phys. Lett.* **118**, 202403 (2021).
- [12] D. Bedau, M. Kläui, S. Krzyk, U. Rüdiger, G. Faini, and L. Vila, *Phys. Rev. Lett.* **99**, 146601 (2007).
- [13] A. Yamaguchi, H. Miyajima, T. Ono, Y. Suzuki, and S. Yuasa, *Appl. Phys. Lett.* **91**, 132509 (2007).
- [14] L. Liu, T. Moriyama, D. C. Ralph, and R. A. Buhrman, *Phys. Rev. Lett.* **106**, 036601 (2011).
- [15] U. H. Pi, K. Won Kim, J. Y. Bae, S. C. Lee, Y. J. Cho, K. S. Kim, and S. Seo, *Appl. Phys. Lett.* **97**, 162507 (2010).
- [16] L. Zhu, D. C. Ralph, and R. A. Buhrman, *Phys. Rev. Lett.* **122**, 077201 (2019).
- [17] M. Aoki, E. Shigematsu, M. Matsushima, R. Ohshima, S. Honda, T. Shinjo, M. Shiraishi, and Y. Ando, *Phys. Rev. B* **102**, 174442 (2020).
- [18] L. Zhu, L. Zhu, and R. A. Buhrman, *Phys. Rev. Lett.* **126**, 107204 (2021).
- [19] J. C. Sankey, Y.-T. Cui, J. Z. Sun, J. C. Slonczewski, R. A. Buhrman, and D. C. Ralph, *Nat. Phys.* **4**, 67 (2008).
- [20] H. Kubota, A. Fukushima, K. Yakushiji, T. Nagahama, S. Yuasa, K. Ando, H. Maehara, Y. Nagamine, K. Tsunekawa, D. D. Jayaprawira, N. Watanabe, and Y. Suzuki, *Nat. Phys.* **4**, 37 (2008).
- [21] T. Devolder, *Phys. Rev. B* **96**, 104413 (2017).
- [22] E. Auerbach, D. Berkov, B. Pichler, N. Leder, H. Arthaber, and S. Gider, *Phys. Rev. Appl.* **12**, 054022 (2019).
- [23] A. Sidi El Valli, V. Iurchuk, G. Lezier, I. Bendjeddou, R. Lebrun, N. Lamard, A. Litvinenko, J. Langer, J. Wrona, L. Vila, R. Sousa, I. L. Prejbeanu, B. Dieny, and U. Ebels, *Appl. Phys. Lett.* **120**, 012406 (2022).
- [24] L. H. Bai, Y. S. Gui, A. Wirthmann, E. Recksiedler, N. Mecking, C. M. Hu, Z. H. Chen, and S. C. Shen, *Appl. Phys. Lett.* **92**, 032504 (2008).
- [25] Z. Feng, J. Hu, L. Sun, B. You, D. Wu, J. Du, W. Zhang, A. Hu, Y. Yang, D. M. Tang, B. S. Zhang, and H. F. Ding, *Phys. Rev. B* **85**, 214423 (2012).
- [26] A. Azevedo, L. H. Vilela-Leão, R. L. Rodríguez-Suárez, A. F. Lacerda Santos, and S. M. Rezende, *Phys. Rev. B* **83**, 144402 (2011).
- [27] L. Bai, P. Hyde, Y. S. Gui, C. M. Hu, V. Vlaminc, J. E. Pearson, S. D. Bader, and A. Hoffmann, *Phys. Rev. Lett.* **111**, 217602 (2013).
- [28] O. Mosendz, J. E. Pearson, F. Y. Fradin, G. E. W. Bauer, S. D. Bader, and A. Hoffmann, *Phys. Rev. Lett.* **104**, 046601 (2010).
- [29] W. Zhang, B. Peng, F. Han, Q. Wang, W. T. Soh, C. K. Ong, and W. Zhang, *Appl. Phys. Lett.* **108**, 102405 (2016).
- [30] F. Huang, W. Zhang, B. Peng, and W. Zhang, *J. Magn. Magn. Mater.* **492**, 165675 (2019).
- [31] Q. Liu, Y. Zhang, L. Sun, B. Miao, X. R. Wang, and H. F. Ding, *Appl. Phys. Lett.* **118**, 132401 (2021).
- [32] S. Martin-Rio, C. Frontera, A. Pomar, L. Balcells, and B. Martinez, *Sci. Rep.* **12**, 224 (2022).
- [33] S. Karimeddiny, J. A. Mittelstaedt, R. A. Buhrman, and D. C. Ralph, *Phys. Rev. Appl.* **14**, 024024 (2020).
- [34] M. Obstbaum, M. Härtinger, H. G. Bauer, T. Meier, F. Swientek, C. H. Back, and G. Woltersdorf, *Phys. Rev. B* **89**, 060407(R) (2014).
- [35] Y. Huo, F. L. Zeng, C. Zhou, and Y. Z. Wu, *Phys. Rev. Appl.* **8**, 014022 (2017).
- [36] U. Chaudhuri, R. Mahendiran, and A. O. Adeyeye, *Appl. Phys. Lett.* **115**, 022406 (2019).
- [37] Q. Zhang, X. Fan, H. Zhou, W. Kong, S. Zhou, Y. S. Gui, C. M. Hu, and D. Xue, *Appl. Phys. Lett.* **112**, 092406 (2018).
- [38] L. Chen, F. Matsukura, and H. Ohno, *Nat. Commun.* **4**, 2055 (2013).
- [39] W. T. Soh, X. Zhong, and C. K. Ong, *Appl. Phys. Lett.* **105**, 112401 (2014).
- [40] J. Lustikova, Y. Shiomi, and E. Saitoh, *Phys. Rev. B* **92**, 224436 (2015).
- [41] S. Keller, J. Greser, M. R. Schweizer, A. Conca, V. Lauer, C. Dubs, B. Hillebrands, and E. T. Papaioannou, *Phys. Rev. B* **96**, 024437 (2017).
- [42] B. B. Singh, K. Roy, J. A. Chelvane, and S. Bedanta, *Phys. Rev. B* **102**, 174444 (2020).
- [43] K. He, J. Cheng, M. Yang, Y. Zhang, L. Yu, Q. Liu, L. Sun, B. Miao, C. Hu, and H. Ding, *Phys. Rev. B* **105**, 104406 (2022).
- [44] R. N. Simons and R. K. Arora, *IEEE Trans. Microwave Theory Tech.* **30**, 1094 (1982).
- [45] R. Iguchi and E. Saitoh, *J. Phys. Soc. Jpn.* **86**, 011003 (2016).
- [46] W. G. Egan and H. J. Juretschke, *J. Appl. Phys.* **34**, 1477 (1963).
- [47] N. Mecking, Y. S. Gui, and C. M. Hu, *Phys. Rev. B* **76**, 224430 (2007).
- [48] M. Harder, Z. X. Cao, Y. S. Gui, X. L. Fan, and C. M. Hu, *Phys. Rev. B* **84**, 054423 (2011).
- [49] J. Cheng, K. He, M. Yang, Q. Liu, R. Yu, L. Sun, J. Ding, B. Miao, M. Wu, and H. F. Ding, *Phys. Rev. B* **103**, 014415 (2021).
- [50] A. Azevedo, O. A. Santos, R. O. Cunha, R. Rodríguez-Suárez, and S. M. Rezende, *Appl. Phys. Lett.* **104**, 152408 (2014).
- [51] A. Tsukahara, Y. Ando, Y. Kitamura, H. Emoto, E. Shikoh, M. P. Delmo, T. Shinjo, and M. Shiraishi, *Phys. Rev. B* **89**, 235317 (2014).